

Timescales of dynamic stall development on a vertical-axis wind turbine blade

Sébastien Le Fouest, Daniel Fernex, and Karen Mulleners*

Institute of Mechanical Engineering, École Polytechnique Fédérale de Lausanne (EPFL), CH-1015 Lausanne, Switzerland

*Corresponding author. E-mail: karen.mulleners@epfl.ch

Abstract

Vertical-axis wind turbines are great candidates to diversify wind energy technology, but their aerodynamic complexity limits industrial deployment. To improve the efficiency and lifespan of vertical axis wind turbines, we desire data-driven models and control strategies that take into account the timing and duration of subsequent events in the unsteady flow development. Here, we aim to characterise the chain of events that leads to dynamic stall on a vertical-axis wind turbine blade and to quantify the influence of the turbine operation conditions on the duration of the individual flow development stages. We present time-resolved flow and unsteady load measurements of a wind turbine model undergoing dynamic stall for a wide range of tip-speed ratios. Proper orthogonal decomposition is used to identify dominant flow structures and to distinguish six characteristic stall stages: the attached flow, shear-layer growth, vortex formation, upwind stall, downwind stall, and flow reattachment stage. The timing and duration of the individual stages are best characterised by the non-dimensional convective time. Dynamic stall stages are also identified based on aerodynamic force measurements. Most of the aerodynamic work is done during the shear-layer growth and the vortex formation stage which underlines the importance of managing dynamic stall on vertical-axis wind turbines.

Impact Statement

Wind energy can play a crucial role in achieving a zero-emission power grid by 2050. One way to increase the installed wind energy capacity is by diversifying wind turbine technologies. Vertical-axis wind turbines are ideal for urban and floating offshore applications, and can complement traditional turbines to achieve higher power density wind farms. Large-scale deployment of vertical-axis wind turbines has been challenging due to their aerodynamic complexity and the occurrence of dynamic stall on the turbine blades. Active flow control can alter the occurrence of dynamic stall on the turbine blade and mitigate load transients. This work aims to characterise the start and duration of landmark dynamic stall stages to facilitate the design of robust, physics-based control laws to improve the performance of vertical-axis wind turbines. The ability to detect transitions between different stages in the flow development using only force measurements is validated.

1. Introduction

Wind power has the potential to play a significant role in reducing the carbon intensity of the global power grid and in reaching the Paris Agreement goal to limit global warming below 2 °C (UNFCCC. *Conference of the Parties (COP), 2015*). A sound strategy to increase the installed wind energy production capacity is to diversify wind energy extraction technologies (Miller et al., 2021; Rolin & Porté-Agel, 2018; Jamieson, 2011). Vertical-axis wind turbines feature many advantages that make them attractive for wind energy exploitation in areas where their horizontal counterparts may face shortcomings, such as urbanised regions or floating offshore applications (De Tavernier et al., 2019; Rezaeiha et al., 2018; Nguyen & Metzger, 2017). These advantages include low noise emissions, high power densities, and insensitivity to wind direction (Buchner et al., 2018; Simão Ferreira et al., 2008). Vertical axis wind-turbines have typically fewer mechanical components than horizontal axis turbines and heavy components such as the drive train and the generator can be placed closer to the ground which facilitates commissioning and maintenance. The performance of wind farms can also be significantly improved by taking advantage of the complementarity of vertical-axis wind turbines and traditional wind turbines (Dabiri, 2011; Strom et al., 2022; Wei et al., 2021).

The development of vertical-axis wind turbines was limited by the complexity of the blade aerodynamics and the resultant lower performance compared to their horizontal counterparts (Rezaeiha et al., 2017; Simão Ferreira et al., 2009; Hwang et al., 2009). Even with steady inflow conditions, the blade inherently undergoes unsteady kinematics. The blade kinematics are often described as the summation of unsteady pitching and surging terms. This description results from a geometric analysis of the problem. The effective flow conditions are expressed using a vectorial sum of the free-stream velocity U_∞ and the blade velocity $U_b = \omega R$, where ω is the turbine rotation frequency, and R is the turbine radius (figure 1). When we consider an azimuthal position $\theta = 0^\circ$ when the blade faces the wind, we can write the variation of the effective velocity as a function of its azimuthal position θ as

$$U_{\text{eff}}(\theta) = \sqrt{1 + 2\lambda \cos \theta + \lambda^2} \quad (1)$$

and the variation of the effective angle of attack as

$$\alpha_{\text{eff}}(\theta) = \tan^{-1} \left(\frac{\sin \theta}{\lambda + \cos \theta} \right) \quad (2)$$

where $\lambda = U_b/U_\infty$ is the tip-speed ratio. The tip-speed ratio is shown to govern the amplitude of the periodic variation in effective flow conditions in equations (1) and (2). For low and medium tip-speed ratios, typically $\lambda < 4.5$, the effective angle of attack exceeds the blade's critical stall angle twice during the rotation, which can lead to flow separation on the blade surface.

The severity of flow separation events increases for decreasing tip-speed ratios. The tip-speed ratio is considered low when the turbine blade exceeds its static stall angle for longer than 4.5 convective times, corresponding to the minimum amount of time required for a coherent leading-edge vortex to form (Dabiri, 2009; Le Fouest et al., 2021; Le Fouest & Mulleners, 2022). Vertical-axis wind turbines operating at low tip-speed ratios ($\lambda \leq 2.5$ when $c/D = 0.2$) undergo deep dynamic stall, which is characterised by the formation, growth, and shedding of large-scale coherent vortices (Carr et al., 1977). The shedding of large-scale vortices is generally followed by a dramatic loss in aerodynamic efficiency and highly unsteady loads that can potentially lead to turbine failure (McCroskey, 1982; Mulleners & Raffel, 2013; Corke & Thomas, 2015).

The temporal occurrence and landmark stages characterising dynamic stall on two-dimensional pitching airfoils in a steady free-stream flow are well documented (Carr et al., 1977; Degani et al., 1998; Mulleners & Raffel, 2013) and their load responses can be reasonably well modelled (Leishman & Bcddoes, 1989; Goman & Khrabrov, 1994; Ayancik & Mulleners, 2022). For a rotating wind turbine

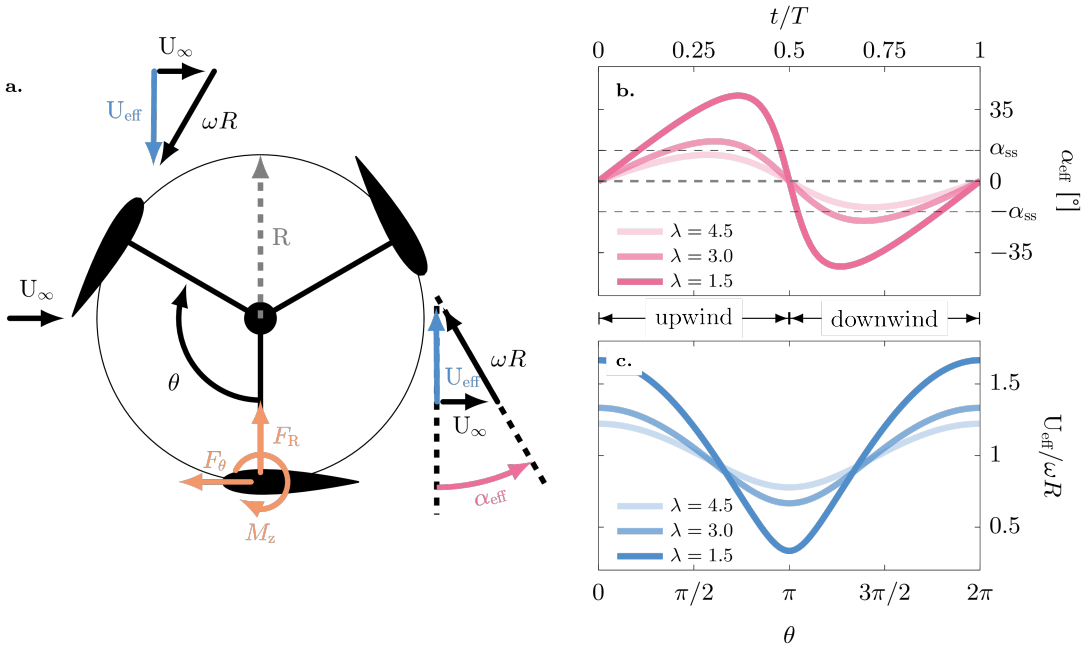


Figure 1. Vertical-axis wind turbine blade kinematics. (a) The free stream velocity U_{∞} goes from left to right. Indication of the positive direction of the radial force F_R , azimuthal force F_{θ} , and pitching moment at quarter-chord M_z . The blade's velocity is equivalent to the rotational frequency ω times the turbine's radius R . Schematic representation of the definition of the blade's effective angle of attack α_{eff} and velocity U_{eff} and their temporal evolution (respectively in (b) and (c)) as a function of the blade's azimuthal position.

blade, the occurrence of dynamic stall is affected by the circularity of the blade's path in several ways. The dynamic stall vortex is convected downstream along the blade's path after it is shed, extending the blade-vortex interaction compared to a blade pitching in a steady flow. The flow topology is dominated by the extended presence of a dissipating dynamic stall vortex at the overlap between the upwind and downwind halves of the blade rotation when the effective velocity is at its lowest (figure 1) (Simão Ferreira et al., 2009; Dave & Franck, 2021). The flow and wake curvature also influence the effective flow acting on a vertical-axis wind turbine blade, leading to virtual camber and incidence effects (Migliore et al., 1980; Benedict et al., 2016). The blade crosses the same stream tube twice, leading to repeated blade-wake interactions even for a single-blade configuration (Fujisawa & Shibuya, 2001; Paraschivoiu, 1988). Typical descriptions of effective flow conditions on a turbine blade, based on equations (1) and (2) do not faithfully capture the complexity of the events unfolding during the blade's rotation, even when coupled with an additional induced velocity term (Paraschivoiu & Delclaux, 1983; Ayati et al., 2019).

Low-order models, such as the actuator cylinder model, improve the prediction of effective flow conditions and unsteady loads by accounting for the velocity induced to the flow by the presence of a rotating turbine (Madsen, 1982). The absence of a reliable dynamic stall model for vertical-axis wind turbines limits the validity of low-order models for low to intermediate tip-speed ratios (Dave et al., 2021). The most widely used dynamic stall models were developed for pitching blades operating in a free stream (Leishman & Bcddoes, 1989; Goman & Khrabrov, 1994). These models rely on a sound understanding of landmark timescales that govern the development of flow separation, namely the vortex formation time and vortex shedding frequency (Ayancik & Mulleners, 2022). For a vertical-axis wind turbine, the timescales of landmark stall events, such as shear layer roll-up or stall onset, have not yet been characterised. Dynamic stall timescales are crucial parameters in the overall design and modelling of

a vertical-axis wind turbine and for more advanced applications such as devising active flow control strategies.

This investigation aims at improving our qualitative and quantitative understanding of the chain of events leading to dynamic stall on a vertical-axis wind turbine blade and the associated timescales. We present time-resolved velocity field and load measurements on a scaled-down H-type Darrieus wind turbine operating in a water channel. A large range of tip-speed ratios is covered to yield a comprehensive characterisation of the occurrence of deep stall on a vertical-axis wind turbine.

2. Experimental materials and methods

The experiments were conducted in a recirculating water channel with a test section of $0.6 \text{ m} \times 0.6 \text{ m} \times 3 \text{ m}$ and a maximum flow velocity of 1 m/s . A cross-sectional view of the full experimental apparatus is shown in [figure 2](#). The main features of the experimental set-up, force and velocity field measurements, and data analysis using proper orthogonal decomposition are summarised here. More details can be found in the supplementary material.

2.1. Experimental set-up

A scaled-down model of a single-bladed H-type Darrieus wind turbine was mounted in the centre of the test section ([figure 2a](#)). The turbine has a variable diameter D that was kept constant at 30 cm . Here, we used the single-blade configuration to focus on the flow development around the blade in the absence of interference from the wakes of other blades. The blade has a NACA0018 profile with a span of $s = 15 \text{ cm}$ and a chord of $c = 6 \text{ cm}$, yielding a chord-to-diameter ratio of $c/D = 0.2$.

The turbine model is driven by a NEMA 34 stepper motor with a 0.05° resolution for the angular position. The rotational frequency was kept constant at 0.89 Hz to maintain a constant chord-based Reynolds number of $\text{Re}_c = (\rho\omega Rc)/\mu = 50\,000$, where ρ is the density and μ the dynamic viscosity of water. To investigate the role of the tip-speed ratio in the occurrence of dynamic stall, we systematically vary the water channel's incoming flow velocity from 0.14 m/s to 0.70 m/s to obtain tip-speed ratios ranging from 1.2 to 6.

2.2. Force measurements

The aerodynamic forces acting on the turbine blade are recorded at 1000 Hz for 100 full turbine rotations using strain gauges that are glued on to the shaft ([figure 2b](#)). The forces presented in this paper are the two shear forces applied at the blade's mid-span in the radial F_R and azimuthal F_θ direction, and the pitching moment about the blade's quarter-chord $M_{1/4}$ ([figure 1](#)). The total force applied to the blade is computed by combining the two shear forces: $F_{\text{tot}} = \sqrt{F_R^2 + F_\theta^2}$. All force coefficients are non-dimensionalised by the blade chord c , the blade span s , and the blade velocity $U_b = \omega R$ such that:

$$C_{\text{tot/R}/\theta} = \frac{F_{\text{tot/R}/\theta}}{0.5\rho U_b^2 s c} \quad . \quad (3)$$

The subscripts tot, R, or θ refer to the total force, the radial, or the tangential force component.

From our load measurements, we retrieve an idealised turbine power coefficient. The instantaneous power P generated by a vertical-axis wind turbine is linearly proportional to the tangential aerodynamic

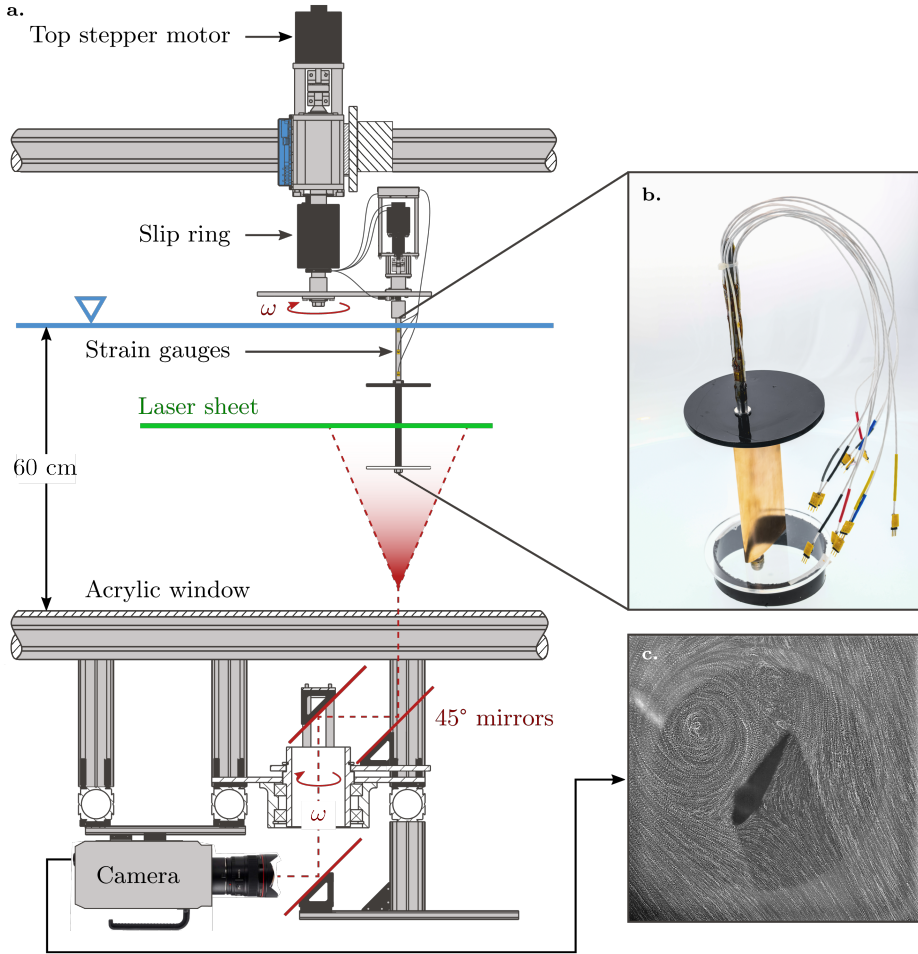


Figure 2. (a) Cross-sectional view of the experimental set-up including the wind turbine model, the light sheet, the rotating mirror system, and the high-speed camera for particle image velocimetry. (b) A close-up view of the blade sub-assembly, with installed strain gauges. (c) The camera's field of view indicated by a long exposure image of seeding particles in the flow.

force experienced by the blade:

$$P(\theta) = F_{\theta} \omega R, \quad (4)$$

where ω is the rotational frequency and R is the turbine's radius. We can calculate the instantaneous power coefficient by normalising the estimated instantaneously generated power by the power available in the flow:

$$C_p(\theta) = \frac{P}{0.5\rho U_{\infty}^3 A_{\text{swept}}}, \quad (5)$$

where A_{swept} is the turbine's swept area given by the product of the turbine diameter and the blade's span. This definition of the power coefficient is idealised because it does not account for any mechanical or electronic losses that would occur on a wind turbine between the turbine blade torque generation and the generator's output.

2.3. Particle image velocimetry

In addition to the blade load measurements, we conducted time-resolved particle image velocimetry (PIV) in the mid-span cross sectional plane of the blade with an acquisition frequency of 1000 Hz. With the help of a rotating mirror system that spins with the same frequency as the wind turbine, we were able to keep a field of view of $2.5c \times 2.5c$ that is centred around the blade (figure 2c).

The particle images were processed following standard procedures using a multi-grid algorithm (Raffel et al., 2007). The final window size was $48 \text{ px} \times 48 \text{ px}$ with an overlap of 75 %. This yields a grid spacing or physical resolution of $1.7 \text{ mm} = 0.029c$. A window overlap above 50 % was selected to minimise spatial averaging of the velocity gradients by the interrogation window following Richard et al. (2006); Kindler et al. (2011). The out-of-plane vorticity component was calculated from the in-plane velocity components using a central difference scheme.

The experimental facility and apparatus were previously described by the authors in Le Fouest & Mulleners (2022). More details on the experimental procedure and the turbine model are provided in the supplementary material.

2.4. Proper orthogonal decomposition

The flow development during a full blade rotation is characterised by significant changes in the flow topology and the formation of vortices when dynamic stall occurs. To identify energetically relevant flow features and their time evolution, we will apply a proper orthogonal decomposition (POD) of the vorticity field. The POD method was introduced to the field of fluid mechanics to identify coherent structures in turbulent flows (Lumley, 2007). The spatial modes ψ_n reveal the dominant and recurring patterns in the data. The corresponding temporal coefficients a_n indicate the dynamic behaviour of the coherent spatial patterns identified in the modes and can be used to extract the characteristic physical timescales of the problem. As the flow under consideration is vortex dominated, we have opted to decompose the vorticity field instead of the velocity field which was used by Dave & Franck (2023). The vorticity field highlights both the rotational and the strain-dominated regions which are both important to understand dynamic stall development (Menon & Mittal, 2021). The POD decomposes the vorticity snapshots at time t_i into a sum of orthonormal spatial modes $\psi_n(x, y)$ and their time coefficients $a_n(t_i)$ such that

$$\omega(x, y, t_i) = \sum_{n=1}^N a_n(t_i) \psi_n(x, y), \quad (6)$$

where N is the total number of snapshots. The POD modes ψ_n form an optimal basis, from which the original system can be reconstructed with the least number of modes compared to any other basis (Sirovich, 1987; Taira et al., 2017).

In this study, we have used the phase-averaged snapshots of the flow field for the PIV analysis to focus on the dynamics within a rotational cycle and to decrease the computational cost of the POD. The dominant POD modes and large-scale vortical structures are similar with both the time-resolved and phase-averaged data. More information about the phase-averaging procedure are included in the supplementary material. The region of interest for the POD analysis covers the entire overlapping measurement field of view which covers the airfoil and the main flow features on each side.

A key aspect of our study is to compare the dominant flow features shared across varying tip-speed ratios and their relative importance for each case. To this purpose, we have stacked five series of 200 phase-averaged vorticity fields $\omega^\lambda(x, y, t_i)$, with $i = 1, \dots, 200$, corresponding to five tip-speed ratios $\lambda \in [1.2, 1.5, 2, 2.5, 3]$ along the time axis into a single matrix $\Omega = \left[\omega^{\lambda=1.2}, \omega^{\lambda=1.5}, \dots, \omega^{\lambda=3} \right]^T$

containing 1000 snapshots. The POD of the combined matrix Ω yields the spatial modes $\psi_n(x, y)$, which are common for all cases. The mode coefficient matrix comprises the mode coefficients corresponding to the individual cases $A = \left[a^{\lambda=1.2}, a^{\lambda=1.5}, \dots, a^{\lambda=3} \right]$. The POD eigenvalues ζ_n indicate the contribution of each mode n to the total energy of the stacked vorticity fields. They are strictly decreasing as POD ranks the modes according to their energy content. With this approach, the vorticity fields for each tip-speed ratio can be reconstructed based on the same set of spatial modes. The temporal contribution of these common structures to individual tip-speed ratios λ is given by the corresponding temporal coefficients a_n^λ . A vorticity field for a specific $\lambda = \lambda_m$ can be reconstructed as

$$\omega^{\lambda=\lambda_m}(x, y, t_i) = \sum_{n=1}^N a_n^{\lambda=\lambda_m}(t_i) \psi_n(x, y) \quad . \quad (7)$$

The energy contribution $\zeta_n^{\lambda=\lambda_m}$ of individual spatial modes $\psi_n(x, y)$ in the tip-speed ratio case $\lambda = \lambda_m$ is computed from the corresponding time coefficients as

$$\zeta_n^{\lambda=\lambda_m} = \left\langle a_n^{\lambda=\lambda_m}, a_n^{\lambda=\lambda_m} \right\rangle = \frac{1}{N_t} \sum_{i=1}^{N_t} \left(a_n^{\lambda=\lambda_m}(t_i) \right)^2 \quad , \quad (8)$$

where $N_t = 200$ is the number of phase-averaged snapshots of the individual tip-speed cases. The procedure used here is similar to the parametric modal decomposition presented by [Coleman et al. \(2019\)](#).

3. Results

3.1. Dynamic stall overview

We first present an overview of the development of flow structures and aerodynamic forces experienced by a vertical-axis wind turbine blade undergoing deep dynamic stall. The temporal evolution of the phase-averaged power coefficient for a wind turbine operating at tip-speed ratio $\lambda = 1.5$ is shown as a polar plot in [figure 3](#). The interplay between the power coefficient and the flow structures forming around the wind turbine blade is highlighted with phase-average vorticity fields presented throughout the blade's rotation. The total aerodynamic force orientation and relative magnitude are represented by an arrow starting from the blade's quarter-chord.

When the blade is facing the wind ($\theta = 0^\circ$), the flow is attached and vorticity is only present in the blade's wake. The total force is small but increases rapidly when the blade moves upwind. At $\theta = 33^\circ$, the blade's effective angle of attack exceeds its critical static stall angle, which was measured to be $\alpha_{ss} = 13^\circ$, and flow reversal emerges on the suction side of the blade. The shear layer rolls up to form a coherent dynamic stall vortex at the leading edge of the blade. The presence of this leading-edge dynamic stall vortex causes the power coefficient to rise from -0.03 at $\theta = 0^\circ$ to its maximum value of 0.32 at $\theta = 77^\circ$. Thereafter, the dynamic stall vortex continues to grow in size and strength and it moves from the leading edge towards the mid-chord position. This migration redirects the aerodynamic force in the radial direction and the power coefficient rapidly drops when the vortex detaches from the blade around $\theta = 114^\circ$. After lift-off, the stall vortex is convected downstream along the blade's path, dissipates, and breaks apart into smaller scale structures. The massive flow separation leads to a drop in the total forces acting on the blade and a collapse of the power production. The power coefficient remains around its minimum value of -0.14 between $\theta = 150^\circ$ and $\theta = 180^\circ$. During the downwind half of the blade's rotation ($180^\circ \leq \theta < 360^\circ$), there is a reversal between the suction and pressure sides of the blade. A second counter-rotating leading-edge vortex now forms on the extrados of the blade's

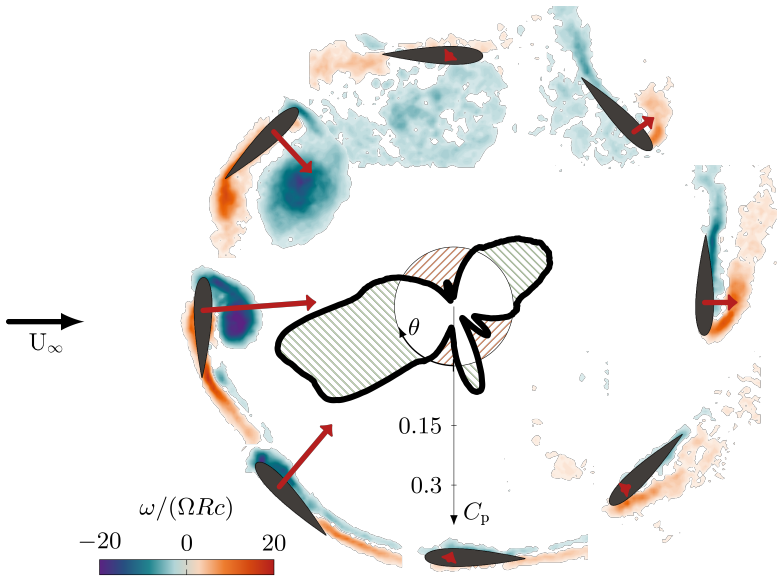


Figure 3. Polar plot of the temporal evolution of the phase-averaged power coefficient C_p for a vertical axis wind turbine operating at tip-speed ratio $\lambda = 1.5$. Phase-averaged normalised vorticity fields are shown throughout the blade's rotation. The total aerodynamic force acting on the blade at the various azimuthal locations is depicted by arrows starting from the blade's quarter-chord. The length of the arrows indicates the relative magnitude of the force. The black circle indicates $C_p = 0$. The hatched regions \square and \square respectively represent regions where the blade experiences net thrust or net drag.

circular path ($\theta = 240^\circ$). This vortex is less coherent and less strong than the one formed during the upwind. It still yields a local maximum in the power coefficient around 0.1. The second leading edge vortex does not remain bound to the blade for long and before we reach $\theta = 270^\circ$, a layer of negative vorticity is entrained between the vortex and the blade surface. The lift-off of the second leading edge vortex leads again to a drop in the power coefficient below 0. The power coefficient reaches a local minimum of -0.07 at $\theta = 329^\circ$. This phase position corresponds to the moment when the blade's angle of attack returns below its critical stall angle and flow reattachment is initiated.

Dynamic stall plays a central role in the temporal evolution of the power coefficient for vertical-axis wind turbines operating at low tip-speed ratios. For all cases with $\lambda \leq 2.4$ in our configuration, we observe a succession of six characteristic stages, including attached flow, shear layer growth, upwind vortex formation, upwind stall, downwind stall, and flow reattachment. The wind turbine's performance varies significantly from one stage to the next. Here, we focus on the characterisation of the temporal development of the flow structures during the full dynamic stall life cycle, their influence on the unsteady load response and turbine power production, and changes in the life cycle as a function of the tip-speed ratio.

3.2. Proper orthogonal decomposition and modal analysis

We use the proper-orthogonal decomposition (POD) of the vorticity field to identify the energetically dominant spatial modes that characterise the flow around our vertical-axis wind turbine blade. The POD time coefficients associated with the dominant spatial modes are examined to identify the characteristic

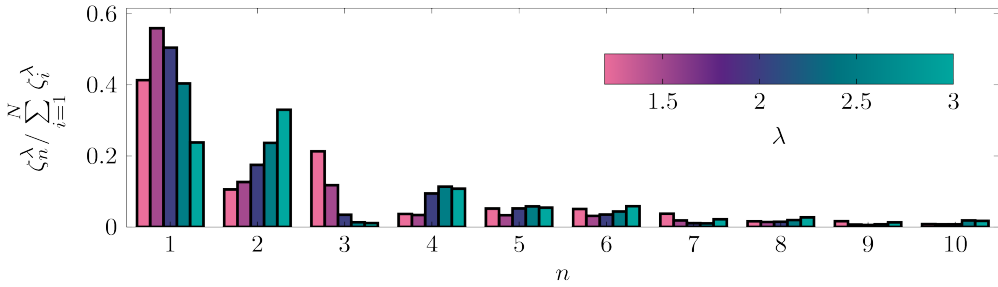


Figure 4. Normalised eigenvalues associated with the first ten spatial POD modes for different tip-speed ratios calculated according to equation (8).

dynamic stall timescales. A single set of spatial eigenmodes is extracted from the ensemble of phase-averaged vorticity fields measured at different tip-speed ratios following the procedure described in section 2.4.

The eigenvalues ζ_n^λ associated with the first ten spatial POD modes for different tip-speed ratios are presented in figure 4. The tip-speed ratio specific eigenvalues are calculated according to equation (8) and represent the energy contribution of the individual spatial modes in the vorticity field reconstruction for the specific tip-speed ratio. The eigenvalues are normalised by the sum of the tip-speed-ratio-specific eigenvalues. Overall, the energy contribution of the modes decreases rapidly with increasing mode number and the first three modes represent more than 70 % of energy for all tip-speed ratios. Analysing flow structures with POD requires striking a balance between conciseness and completeness. Selecting too few modes means one might ignore a too large energetic portion of the flow, while selecting too many sacrifices the benefits of a low-order analysis. Here, we focus on the first three spatial modes to analyse the temporal development of dominant flow features.

The first three spatial POD modes are presented in figure 5. The corresponding time coefficients are shown for tip-speed ratios $\lambda = 1.2, 1.5, 2.0, 2.5$ and 3.0 . The time coefficients a_n are normalised by the eigenvalues obtained from the stacked flow field POD (section 2.4). The first spatial mode is characterised by the presence of a large dynamic stall vortex with a vortex centre located at mid-chord and half-chord length above the blade’s surface. Note that the modes are presented in the blade’s frame of reference. Everything that is above the blade corresponds to what happens on the intrados of the blade’s rotational trajectory. The temporal evolution of the corresponding time coefficient a_1 shows a distinctive peak when the upwind dynamic stall vortex is prominent. The amplitude of the peak increases with decreasing tip-speed ratio. The increase in amplitude highlights a more dominant large-scale vortex for decreasing tip-speed ratio. At lower tip-speed ratios, the maximum effective angle of attack increases (figure 1) and the strength of the dynamic stall vortex increases (Le Fouest & Mulleners, 2022). The first POD mode and the corresponding time coefficient can be used to characterise the timescales related to the formation of the upwind dynamic stall vortex.

The interpretation of the second spatial POD mode is more intricate than the first one, as it seems to combine two consecutive events that occur in the flow. The time coefficient a_2 is negative at the start of the upwind and initially decreases for all cases ($0 \leq t/T < 0.25$). During this time period, flow reversal is first observed on the suction side of the turbine blade or the intrados of the blade’s rotational trajectory. Once the blade exceeds its critical stall angle, the time coefficient a_2 starts to increase, becomes positive, and peaks at the occurrence of vortex lift-off. The increase in a_2 can be interpreted as the transition from a strong accumulation of negative vorticity near the surface during flow reversal, to the growth of a large vortex that entrains positive vorticity near the surface that leads to separation of the main upwind stall vortex. The positive peak of the second mode coefficient occurs at the same time as the negative peak of the first mode coefficient. The first two modes do not form a classical mode pair, where

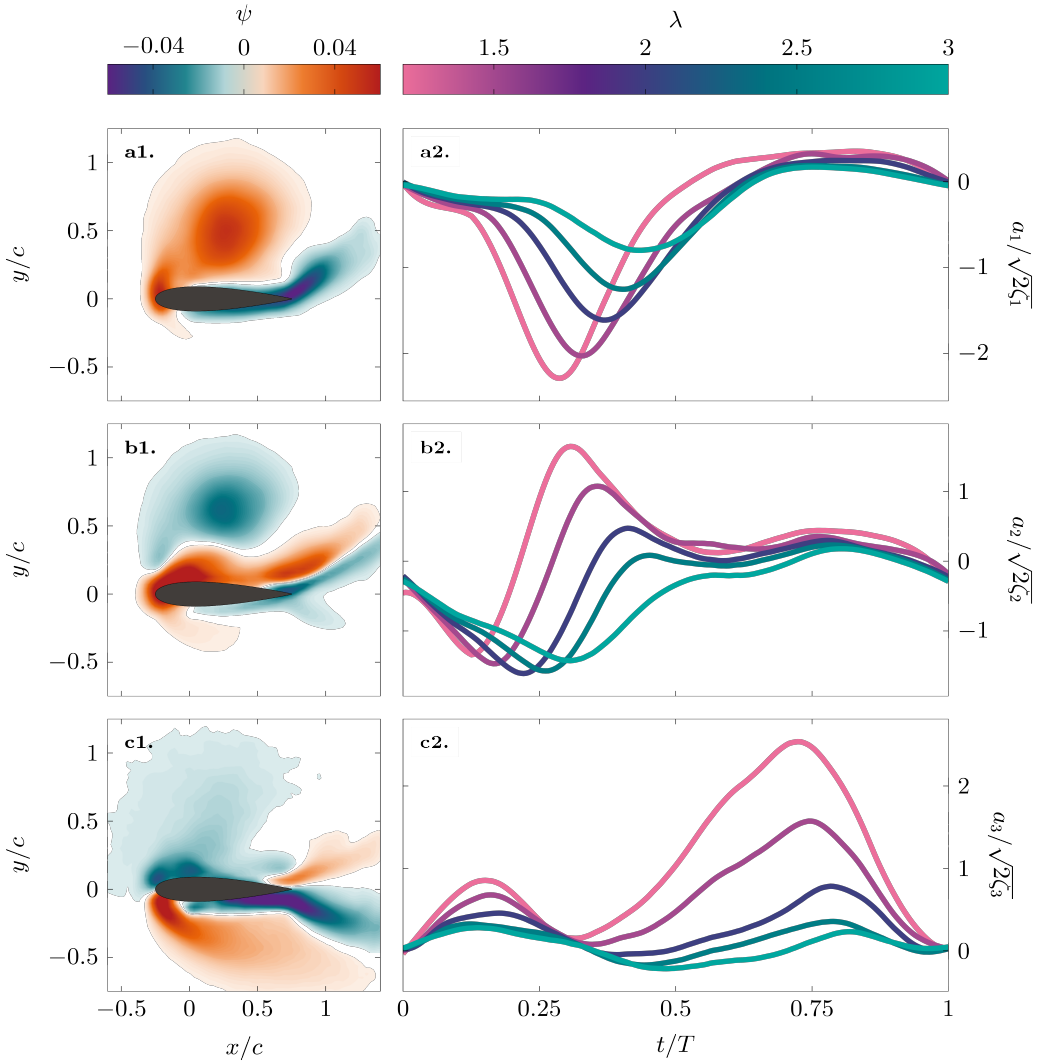


Figure 5. First three spatial POD modes (a1-c1) and the evolution of the corresponding time coefficients for tip-speed ratios $\lambda = 1.2, 1.5, 2.0, 2.5$ and 3.0 (a2-c2).

energy is transferred from one to the other, they rather reinforce each other. The second POD mode and the corresponding time coefficient can be used to characterise the transition from the accumulation of vorticity and growth of the shear layer to the roll-up of the shear layer into a large-scale upwind dynamic stall vortex.

The third spatial POD mode does not display the presence of a coherent flow structure but rather a state of massively separated flow. The corresponding time coefficient a_3 significantly increases immediately after the separation of the upwind stall vortex, which corresponds to the moment when the amplitude of the first time coefficient a_1 decreases. The third spatial mode represents the fully separated flow following vortex detachment. The severity of the post-stall conditions increases with decreasing tip-speed ratio. Low tip-speed ratio cases are characterised by the formation of a stronger dynamic stall vortex than intermediate and high tip-speed ratio cases and they experience more pronounced deep stall events. The absence of a coherent flow structure in the third spatial mode explains the asymmetry in

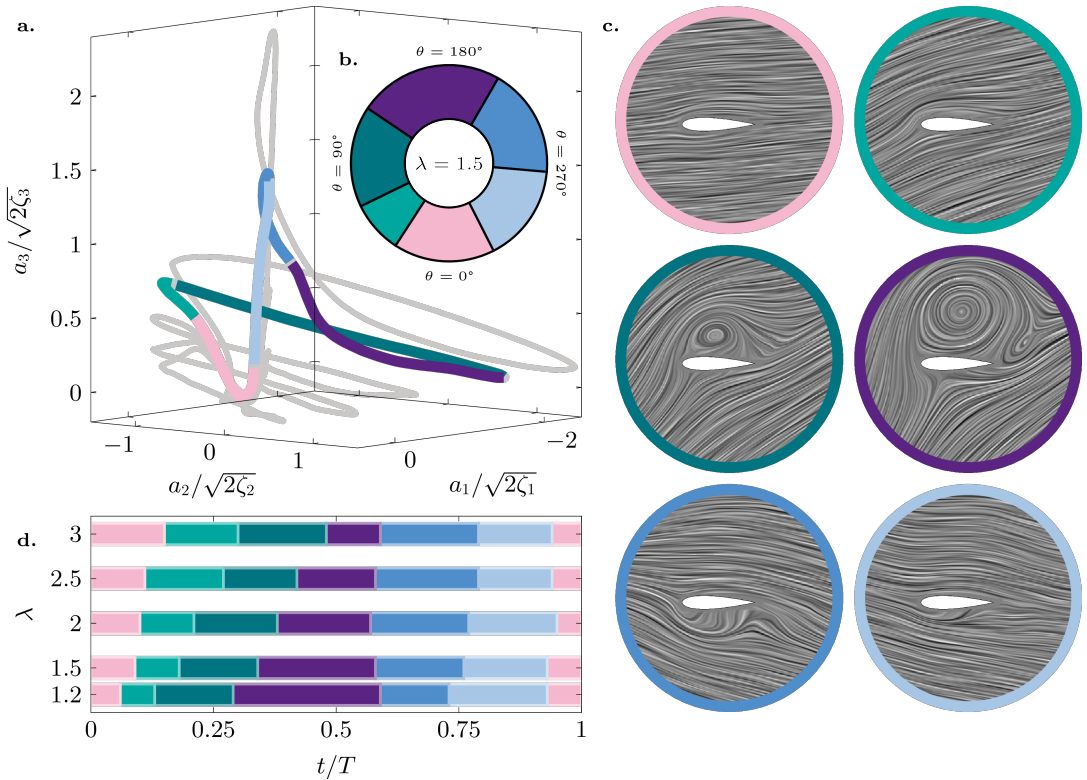


Figure 6. (a) Time coefficient parametric curve obtained from the stacked vorticity field POD (section 2.4). The inset (b) shows the phase map of the characteristic dynamic stall stages experienced by the wind turbine blade operating at tip-speed ratio $\lambda = 1.5$. The stages are: attached flow █, shear layer growth █, vortex formation █, upwind stall █, downwind stall █, and flow reattachment █. (c) Selected snapshots of the flow topology representing the characteristic stall stages obtained by the line integral convolution method. (d) Duration and timing of the dynamic stall stages for tip-speed ratio cases $\lambda = 1.2, 1.5, 2.0, 2.5$ and 3.0 .

power production between the upwind and downwind halves of the rotation presented exemplarily in figure 3. During upwind, a torque-producing coherent leading-edge vortex is formed. During downwind, the flow is massively separated and the loads are characterised by drag excursions.

The time coefficients of the first three POD modes will be used next to identify the timing of the different dynamic stall stages. The fourth POD mode, which plays a more prominent role than the third mode for higher tip-speed ratios where stall is less prominent, did not provide additional information for the identification of the stall stages. It is included for reference in the supplementary material.

3.3. Identification of dynamic stall stages using POD time coefficients

The trajectories in the feature space spanned by the POD time coefficients corresponding to the three dominant modes are shown in figure 6a for tip-speed ratio cases $\lambda = 1.2, 1.5, 2.0, 2.5$ and 3.0 . The trajectory corresponding to the tip-speed ratio $\lambda = 1.5$ is colour-coded and used as an example to demonstrate our approach to identifying the timing of the various stages in the flow development. The feature space representation highlights the interplay between the time coefficients. We analyse the points of inflection of the trajectory. A change in the relative importance of the time coefficient

creates an inflection point on the trajectory in the feature space and relates to key events in the flow development. The inflection points were systematically compared to the phase-averaged flow fields to determine their physical significance. The results presented here are manually extracted and subject to the authors' discretion. The inflection points were found by inspecting the three dimensional curves from various orientations. Not all of them are visible in the two dimensional projection depicted in [figure 6a](#). Additional projections are included in the supplementary material.

We identify the timing and duration of six landmark stages: attached flow (■), upwind shear layer growth stage (■), upwind vortex formation stage (■), upwind stalled stage (■), downwind stalled stage (■), and flow reattachment (■). A phase map for the six stages is shown for $\lambda = 1.5$ in [figure 6b](#). Visualisations of the flow topology characteristic of the individual stages are obtained by applying the line integral convolution method (LIC) to phase averaged flow field snapshots ([figure 6c](#)). The timing and duration of the dynamic stall stages are summarised in [figure 6d](#).

The same six stages occur for all tip-speed ratios, but the timing and duration of these stages vary. The flow is attached when the blade enters the upwind part of the rotation for all cases. First signs of stall development occur when the blade exceeds its critical stall angle, which happens later in the cycle for higher tip-speed ratios ([figure 1b](#)). Within less than a quarter of a rotation, a coherent upwind stall vortex has formed, which continues to grow in chord-wise and chord-normal direction until the vortex lifts off and opposite-signed vorticity is entrained between the vortex and the blade's surface. The entrainment of secondary vorticity ultimately leads to the detachment of the stall vortex and the onset of upwind dynamic stall. This process is similar to the vortex-induced separation observed on two-dimensional pitching and plunging airfoils ([Doligalski & Smith, 1994](#); [Mulleners & Raffel, 2012](#); [Rival et al., 2014](#)).

The upwind dynamic stall onset is identified in the POD feature space in [figure 6a](#) as the local maximum of a_2 and the minimum of a_1 . The time interval between the moment when the blade exceeds its critical stall angle and the onset of stall is defined as the upwind stall development. We divide the upwind stall development into two parts in analogy with the flow development observed on pitching airfoils ([Mulleners & Raffel, 2013](#); [Deparday & Mulleners, 2019](#)). The first part is characterised by the accumulation of bound vorticity and the thickening of the surface shear layer. We call this stage the shear layer growth stage. The shear layer growth stage (■) takes up a larger portion of the cycle when the tip-speed ratio increases ([figure 6d](#)). A kink in the feature space at the minimum of a_2 and a local extremum of a_1 marks the start of the roll-up of the shear layer into a coherent dynamic stall vortex. This second part of the upwind stall development is characterised by the growth of the upwind dynamic stall vortex and is called the upwind vortex formation stage. The vortex formation stage (■) occupies approximately the same portion of the cycle for all tip-speed ratios but ends earlier in the cycle for lower tip-speed ratios ([figure 6d](#)). Stall onset marks the end of the vortex formation stage and the start of the upwind stalled stage.

The next transition is marked by the switch of the leading edge stagnation point from the intrados of the blade path to the extrados, which corresponds respectively to the bottom and the top side of the blade in the snapshots presented in [figure 1c](#). This transition is identified in the POD feature space as an inflection point in the gradient of a_3 and occurs at approximately the same point in the cycle ([figure 6d](#)). As the blade enters the downwind half of the rotation, the fully separated flow has no time to reattach to the blade even though the angle of attack is theoretically at 0° when $\theta = 180^\circ$. Furthermore, the blade's angle of attack varies more rapidly in the first part of the downwind than during the upwind. There is insufficient time for a clear shear layer growth and vortex formation stage during the downwind, so we only consider an overall downwind stalled stage ([Le Fouest & Mulleners, 2022](#)). The end of the downwind stalled stage is marked by the maximum value of a_3 and it is followed by the flow reattachment stage. The flow reattaches to the blade for all cases in the last quarter of the turbine's rotation.

The characteristic upwind dynamic stall delay is the combined duration of the shear layer growth and the vortex formations stage. Based on previous work, we expect that the duration of the stall delay expressed

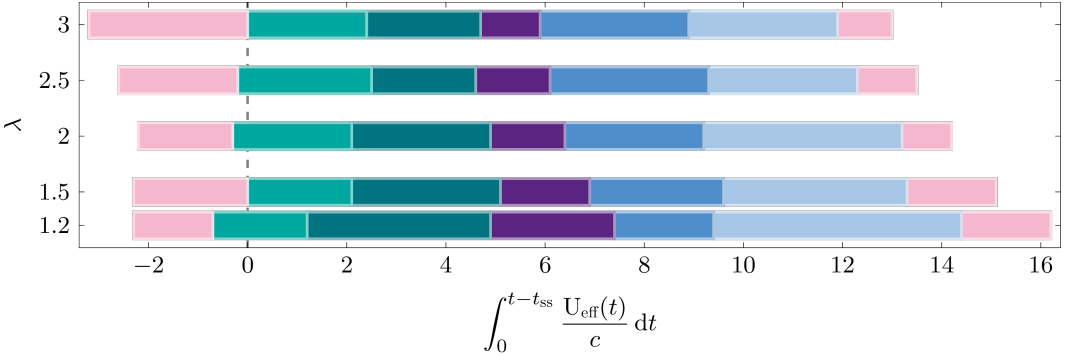


Figure 7. Duration and timing of the dynamic stall stages for tip-speed ratio cases $\lambda = 1.2, 1.5, 2.0, 2.5$ and 3.0 in terms of the convective time. The stages are: attached flow (pink), shear layer growth (teal), vortex formation (dark teal), upwind stall (purple), downwind stall (blue), and flow reattachment (light blue).

in convective time scales becomes independent of the kinematics for larger reduced frequencies (Le Fouest et al., 2021; Ayancik & Mulleners, 2022). Generally, the non-dimensional convective time is obtained by dividing the physical time by c/U , with U a constant characteristic velocity. Here, the effective flow velocity experienced by the blade changes constantly and instead of using the blade velocity or the free-stream velocity to obtain a non-dimensional convective time, we opt here to take the constantly varying effective flow velocity into account and calculate the convective time perceived by the turbine blade using:

$$\int_0^{t-t_{ss}} \frac{U_{\text{eff}}(t)}{c} dt, \quad (9)$$

where U_{eff} is the effective flow velocity obtained from the vectorial combination of the blade velocity and the incoming flow velocity (figure 1).

The temporal occurrence of dynamic stall stages scaled with the convective time is presented in figure 7. Note that we subtract the time at which the static stall angle is exceeded t_{ss} to realign subsequent stall events, in accordance with results presented in Buchner et al. (2018). When we express the upwind stall delay (teal + dark teal) in terms of convective times, the stall delay does not depend on the tip-speed ratio and converges to approximately 4.5 convective times, which matches standard vortex formation times found in literature (Gharib et al., 1998; Dabiri, 2009; Dunne et al., 2016; Kiefer et al., 2022). The combination of the upwind and downwind stalled stages also reaches similar values for all tip-speed ratios, although the distribution between the two stages varies. The flow reattachment timescale decreases slightly for increasing tip-speed ratios. This trend may be due to the discrepancy between the effective flow velocity calculated using equation (1) and the actual effective flow velocity acting on the turbine blade in the downwind half of the turbine rotation. Equation (1) neglects any influence of the induced velocity from shed vorticity, which is abundant in the downwind half of the turbine's rotation. Overall, the convective time offers a promising scaling option for dynamic stall timescales on vertical axis turbines. Further work can aim at modelling the influence of vorticity induced velocity to improve the scaling and implement universal timescales into dynamic stall modelling and control strategies for vertical-axis wind turbines.

3.4. Identification of dynamic stall stages using the aerodynamic loads

We cannot rely on flow measurements if we want to achieve real-time active flow control on a wind turbine blade. The processing time of the flow measurement around the blade, capturing vortex formation or incoming gusts, for instance, is prohibitively high to actuate a response in time. Finding patterns in

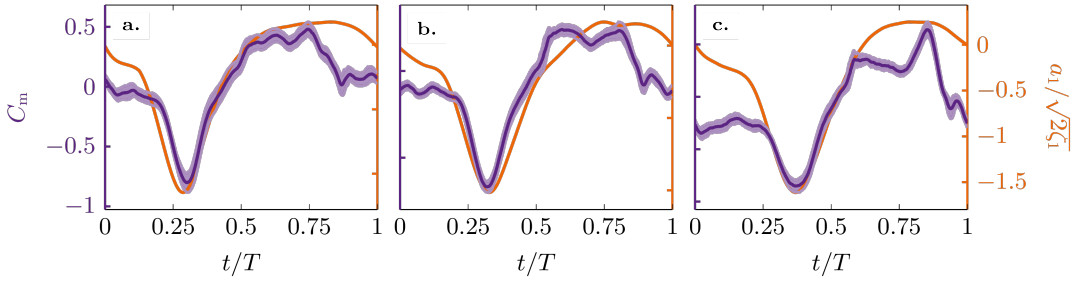


Figure 8. Comparison of the temporal evolution of the first POD mode time coefficient a_1 and the phase-averaged pitching moment coefficient for tip-speed ratio cases $\lambda = 1.2, 1.5, 2.0$.

the readily available aerodynamic loads that indicate the occurrence of stall stages is desirable. This feasibility of replacing the time series of the POD coefficients with load measurement time series was inspired by the similarity between some features in the POD time coefficients and the temporal development of the aerodynamic loads. In figure 8, we compare the temporal evolution of the time coefficient a_1 corresponding to the first POD mode and the phase-averaged pitching moment coefficient for tip-speed ratios $\lambda = 1.2, 1.5, 2.0$. The general shape of the two curves is in close agreement. The timing of the distinctive peak displayed by the time coefficient a_1 perfectly matches the timing of the negative pitching moment peak. The pitching moment is highly sensitive to changes in the formation of the large-scale upwind dynamic stall vortex, which is characterised by the mode coefficient a_1 . This further confirms our interpretation of the first POD mode and motivates us to extract the timing and duration of the dynamic stall stages based solely on the aerodynamic loads.

We analyse the dynamic stall timescales based on the development of the unsteady loads experienced by the wind turbine blade using a similar approach as for the POD time coefficients. Our new feature space is built using the azimuthal force, radial force and pitching moment coefficients and analyse the measured trajectories in figure 9a for 19 tip-speed ratio cases with $\lambda \in [1.2 - 3.0]$. The trajectory corresponding to the tip-speed ratio $\lambda = 1.5$ is colour-coded and used as an example to demonstrate the automated identification of the dynamic stall stages from the unsteady loads. Automated identification increases the robustness and the potential of using unsteady loads as the input for active flow control laws. The points of inflection formed by the unsteady load trajectories are not as clearly defined as those in the POD time coefficient trajectory shown in figure 5a, but we are able to identify five extrema that are systematically featured in the temporal development of the aerodynamic loads and that can be directly related to the changes in the dynamic stall life cycle. These extrema were identified by closely analysing the interplay between flow structures developing around the turbine blade and abrupt changes in the load response.

The first extremum we identified is the tangential force minimum occurring shortly after the blade enters the upwind half of its rotation ($0 \leq t/T < 0.5$) (figure 9b). This time instant is followed by a strong increase in torque production, which corresponds to the shear-layer growth stage (figure 3, $\theta = 45^\circ$). The end of the shear-layer growth stage coincides with the tangential force maximum occurring around $t/T = 0.25$. The vortex formation stage is characterised by the convection of the upwind dynamic stall vortex from the leading edge towards the mid-chord position, causing a significant excursion of the pitching moment coefficient from just below 0 to its minimum value $C_{M,\min}$ (figure 9c). The pitching moment minimum coincides with vortex separation and the beginning of the upwind stalled stage. Vortex separation is followed by a significant loss in radial force that decreases until around $t/T = 0.6$, reaching a plateau that corresponds to the downwind stalled stage. The transition from a sharp decrease to a plateau is identified using the function `findchangepts` in MATLAB. Lastly, the pitching moment coefficient reached a local maximum before returning to its initial value during the flow reattachment stage. These extrema are used to identify the landmark dynamic stall stages for all tip-speed ratio cases $\lambda \in [1.2 - 3.0]$.

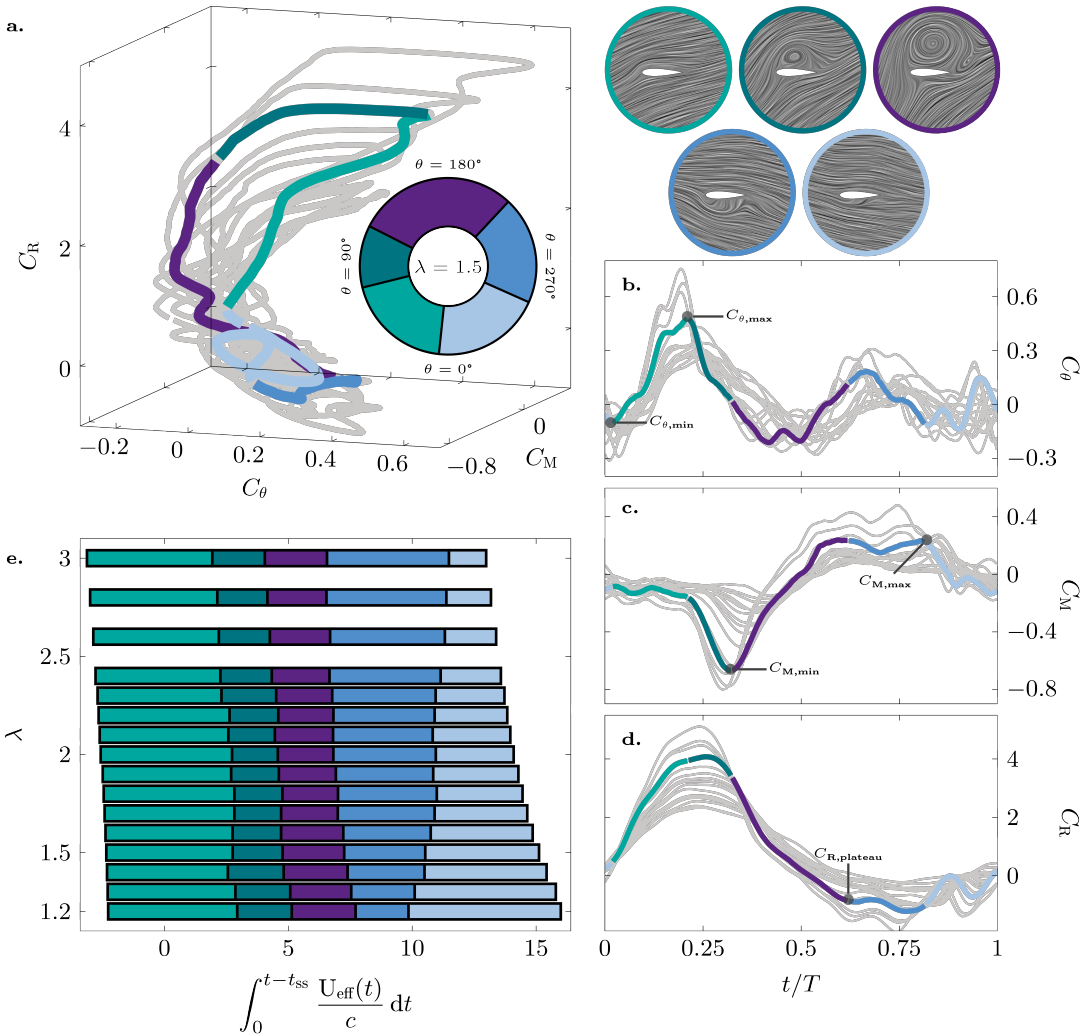


Figure 9. (a) Unsteady force parametric curve for tip-speed ratios $\lambda \in [1.2 - 3.0]$. The inset shows the phase map of the characteristic dynamic stall stages experienced by the wind turbine blade operating at tip-speed ratio $\lambda = 1.5$. The stages are: attached flow and shear layer growth ■, vortex formation ■, upwind stall ■, downwind stall ■, and flow reattachment ■. (b) Duration and timing of the dynamic stall stages retrieved from the unsteady loads for tip-speed ratio $\lambda \in [1.2 - 3.0]$. Temporal evolution of phase-averaged unsteady (c) tangential load coefficient C_θ , (d) pitching moment coefficient C_M , (e) radiant force coefficient C_R for tip-speed ratios $\lambda \in [1.2 - 3.0]$. Selected snapshots of the flow topology representing the characteristic stall stages are repeated as reminders.

A phase map showing the temporal occurrence of dynamic stall stages identified using unsteady loads is shown as an inset in figure 9a for $\lambda = 1.5$. The stages we identify from loads are the same as those identified using the time coefficient of the vorticity field POD with one exception: the attached flow stage. There is no clear indication of an attached stage in the unsteady load response. The blade experiences an immediate load response to the increase of the effective angle of attack at the beginning of the blade's rotation, but the appearance of flow reversal and shear-layer growth is delayed to higher angles of attack. The first stage (■) shown in figure 9e thus combines the attached flow stage and the shear layer growth stage. The timing and duration of the following stages match those computed

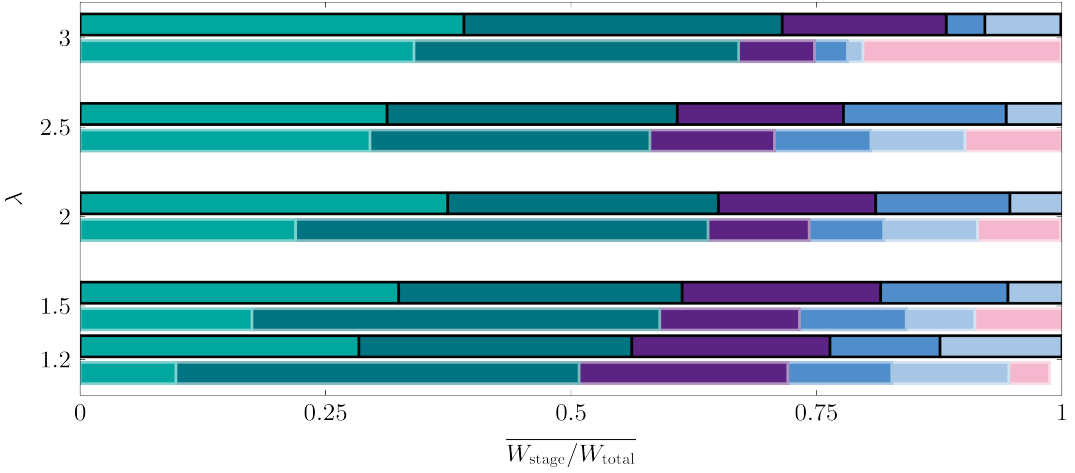


Figure 10. Stage-wise contribution to the total work completed by the total aerodynamic force throughout the blade's rotation. The stage contributions are compared for stages identified either by using aerodynamic loads (dark contours) or by using POD time coefficients (light contours) for tip-speed ratios $\lambda = [1.2, 1.5, 2.0, 2.5 \text{ and } 3.0]$. The stages are: attached flow █, shear layer growth █, vortex formation █, upwind stall █, downwind stall █, and flow reattachment █.

with the POD time coefficients. These findings suggest that the aerodynamic loads contain sufficient information to identify whether a wind turbine blade is undergoing dynamic stall and which stage the flow development is currently in.

3.5. Stage-wise comparison of both identification methods

A direct comparison of both stage identification methods is desirable to assess the potential of unsteady loads to capture the timescales of flow development for analytical or control purposes. To allow for a direct comparison between the stages computed from the aerodynamic loads and those obtained using the POD time coefficients, we calculated the work done by the total aerodynamic force in each stage for both methods. The work done by the total aerodynamic force over a given stage is calculated with:

$$W_{\text{stage}} = \overline{F_{\text{tot}}} \Theta_{\text{stage}} R \quad (10)$$

where $\overline{F_{\text{tot}}}$ is the mean total aerodynamic force experienced by the turbine blade over that stage and Θ_{stage} is the angular distance covered by the blade throughout the stage. This metric allows a pertinent comparison between the two stage identification methods because it accounts for both the duration of the stage and the magnitude of the loads experienced by the turbine blade during that stage. A small error in the timescale of a given stage is enhanced if the stage is related to significant unsteady loads. Alternatively, we could have chosen the blade's time-averaged power production over each stage as a metric, but we preferred the work done by the total force because it accounts for both the radial and tangential force components and has a high signal-to-noise ratio, even for high tip-speed ratio cases when the force magnitude is lower.

The stage-wise contributions to the work completed by the aerodynamic force are compared in [figure 10](#) for stages identified using either the aerodynamic loads or the POD time coefficients for tip-speed ratios $\lambda = [1.2, 1.5, 2.0, 2.5 \text{ and } 3.0]$. To facilitate the comparison, the work completed in each stage W_{stage} is normalised by the total work completed by the aerodynamic force throughout the blade's rotation $W_{\text{total}} = \overline{F_{\text{tot}}} 2\pi R$.

Overall, most of the aerodynamic work is completed during the shear layer growth (■) and the vortex formation stage (■). These stages are associated with the accumulation of vorticity close to the blade's surface, which creates significant suction over about one quarter of the turbine's rotation. This trend is verified for both stage identification methods at all tip-speed ratios. The combined contribution of the shear layer growth and the vortex formation stage is nearly independent of tip-speed ratio and reaches 0.6 for all cases. Both stage identification methods show excellent agreement. The aerodynamic loads do not allow for a clear identification of the attached flow stage. Instead, the attached flow stage is distributed across the flow reattachment and mainly the shear layer growth stages. The work contribution of the attached flow stage is limited across tip-speed ratios. The accurate capture of key timescales, such as the vortex formation time, is a satisfactory and promising result for the use of aerodynamic loads as a tool to identify flow development timescales and implement closed-loop control strategies.

4. Conclusion

We collected time-resolved velocity field and unsteady load measurements on a vertical-axis wind turbine operating at low tip-speed ratios $\lambda \in [1.2 - 3.0]$ to characterise the chain of events that leads to dynamic stall and to quantify the influence of the turbine operation conditions on the duration of the individual stages of the flow development. The dominant flow features and their timescales were first analysed using a proper orthogonal decomposition of the stacked vorticity fields from different tip speed ratio conditions. This procedure is known as a parametric modal decomposition and yields a single set of representative spatial modes and tip-speed ratio specific temporal coefficients and eigenvalues that can be directly compared to characterise the influence of the tip-speed ratio on the temporal development of the dominant spatial flow features.

Based on the POD time coefficients of the three most energetic modes, we were able to identify the timing and duration of six landmark dynamic stall stages: the attached flow, shear layer growth, vortex formation, upwind stall, downwind stall, and flow reattachment stage. The duration of the attached flow increases with increasing tip-speed ratio as the blade exceeds its critical stall angle later for higher tip-speed ratios. The combined duration of the shear layer growth and vortex formation stages represent the characteristic dynamic stall delay. This dynamic stall delay is independent of tip-speed ratio for our experimental conditions and reaches a constant non-dimensional value of 4.5 convective times, which corresponds to the typical dynamic stall delays found on non-rotating pitching and plunging airfoils at comparable reduced frequencies. The upwind and downwind stall stages shorten with increasing tip-speed ratio as the blade spends less time at angles of attack beyond the critical stall angle. Flow reattachment starts once the blade returns below its critical angle and full reattachment is reached within 3 to 4 convective times for all cases studied. The dynamic stall stages were also identified based solely on the measured aerodynamic loads. The timing of the dynamic stall stages based on the loads agrees well with the timing based on the time coefficients of the first three modes of the POD of the vorticity field.

Our findings demonstrate that aerodynamic loads are suitable for analysing the timescales of flow development on a vertical axis wind turbine blade and can be used for flow control applications. However, a control strategy should not necessarily aim at avoiding the onset of dynamic stall as the work completed by the aerodynamic forces during the upwind dynamic stall delay represents approximately 60 % of the total work completed throughout the turbine's rotation. Future work should focus on careful management of the dynamic stall vortex formation and shedding to exploit the work done by the vortex but avoid potential negative ramifications related to its shedding.

Funding Statement. Support from the Swiss national science foundation under grant number PYAPP2_173652 is gratefully acknowledged.

Declaration of Interests. The authors declare no conflict of interest.

Data Availability Statement. The data used in this work will be made available upon request.

References

- Roshko, A. (1961). Experiments on the flow past a circular cylinder at very high Reynolds number. *Journal of Fluid Mechanics*, 10(3), 345–356, 1469-7645.
- Carr, L. W., Mcalister, K. W., & Mccroskey, W. J. (1977). Analysis of Dynamic Oscillating the Development Stall Based on Airfoil Experiments. Technical report, National Aeronautics and Space Administration.
- Migliore, P. G., Wolfe, W. P., & Fanucci, J. B. (1980). Flow Curvature Effects on Darrieus Turbine Blade Aerodynamics. *Journal of energy*, 4(2), 49–55, 01460412.
- Madsen, H. A. (1982). *The actuator cylinder - a flow model for vertical axis wind turbine*. Ph.D. thesis, Aalborg University, Denmark.
- Mccroskey, W. J. (1982). Unsteady airfoils. pages 285–311.
- Paraschivoiu, I. & Delclaux, F. (1983). Double multiple streamtube model with recent improvements (for predicting aerodynamic loads and performance of Darrieus vertical axis wind turbines). *Journal of Energy*, 7(3), 250–255, 0146-0412.
- Sirovich, L. (1987). Turbulence and the dynamics of coherent structures. II. symmetries and transformations. *Quarterly of Applied Mathematics*, 45(3), 573–582.
- Paraschivoiu, I. (1988). Double-Multiple Streamtube Model for Studying Vertical-Axis Wind Turbines. *Journal of Propulsion and Power*, 4(4), 370–378.
- Leishman, J. G. & Bcdoes, T. S. (1989). A semi-empirical model for dynamic stall. *Journal of the American Helicopter Society*, 34(3), 3–17, 00028711.
- Doligalski, T. L. & Smith, C. R. (1994). Vortex interactions with walls. *Annual Review of Fluid Mechanics*, 26, 573 616.
- Goman, M. & Khrabrov, A. (1994). State-Space Representation of Aerodynamic Characteristics of an Aircraft at High Angles of Attack. *Journal of Aircraft*, 31(5), 1109–1115.
- Degani, A. T., Walker, J. D., & Smith, F. T. (1998). Unsteady separation past moving surfaces. *Journal of Fluid Mechanics*, 375, 1–38, 1469-7645.
- Gharib, M., Rambod, E., & Shariff, K. (1998). A universal time scale for vortex ring formation. *Journal of Fluid Mechanics*, 360, 121–140, 1469-7645.
- Fujisawa, N. & Shibuya, S. (2001). Observations of dynamic stall on turbine blades. *Journal of Wind Engineering and Industrial Aerodynamics*, 89(2), 201–214, 01676105.
- Richard, H., Bosbach, J., Henning, A., Raffel, M., Willert, C., & Wall, B. G. v. d. (2006). 2C and 3C PIV measurements on a rotor in hover condition. In *13th International symposium on applications of laser techniques to fluid mechanics*. Lisbon, Portugal.
- Lumley, J. L. (2007). *Stochastic tools in turbulence*. Courier Corporation.
- Raffel, M., Willert, C. E., Wereley, S. T., & Kompenhans, J. (2007). *Particle Image Velocimetry*. Springer Berlin Heidelberg, Berlin, Heidelberg. ISBN 978-3-540-72307-3.
- Simão Ferreira, C., Van Kuik, G., van Bussel, G., & Scarano, F. (2008). Visualization by PIV of dynamic stall on a vertical axis wind turbine. *Experiments in Fluids*, 46(1), 97–108, 07234864.
- Dabiri, J. O. (2009). Optimal Vortex Formation as a Unifying Principle in Biological Propulsion. *Annual Review of Fluid Mechanics*, 41(1), 17–33, 0066-4189.
- Hwang, I. S., Lee, Y. H., & Kim, S. J. (2009). Optimization of cycloidal water turbine and the performance improvement by individual blade control. *Applied Energy*, 86(9), 1532–1540, 03062619.
- Simão Ferreira, C. J., Van Zuijlen, A., Bijl, H., Van Bussel, G., Van Kuik, G., Ferreira, C. J. S., Van Zuijlen, A., Bijl, H., Van Bussel, G., & Van Kuik, G. (2009). Simulating dynamic stall in a two-dimensional vertical-axis wind turbine: verification and validation with particle image velocimetry data. *Wind Energy*, 13(1), 1–17, 1099-1824.
- Dabiri, J. O. (2011). Potential order-of-magnitude enhancement of wind farm power density via counter-rotating vertical-axis wind turbine arrays. *Journal of Renewable and Sustainable Energy*, 3(4), 19417012.
- Jamieson, P. (2011). *Innovation in Wind Turbine Design*. John Wiley and Sons. ISBN 9780470699812.
- Kindler, K., Mulleners, K., Richard, H., van der Wall, B. G., & Raffel, M. (2011). Aperiodicity in the near field of full-scale rotor blade tip vortices. *Experiments in Fluids*, 50(6), 1601–1610, 0723-4864, 1432-1114.
- Mulleners, K. & Raffel, M. (2012). The onset of dynamic stall revisited. *Experiments in Fluids*, 52(3), 779–793, 0723-4864.
- Mulleners, K. & Raffel, M. (2013). Dynamic stall development. *Experiments in Fluids*, 54(2), 1–9, 07234864.
- Rival, D. E., Kriegseis, J., Schaub, P., Widmann, A., & Tropea, C. (2014). Characteristic length scales for vortex detachment on plunging profiles with varying leading-edge geometry. *Experiments in Fluids*, 55, 1660, 0723-4864.
- Corke, T. C. & Thomas, F. O. (2015). Dynamic Stall in Pitching Airfoils: Aerodynamic Damping and Compressibility Effects. *Annual Review of Fluid Mechanics*, 47(1), 479–505, 0066-4189.
- UNFCCC. Conference of the Parties (COP) (2015). Adoption of the Paris Agreement. Proposal by the President. *Paris Climate Change Conference - November 2015, COP 21, 21932*(December), 32, 1098-6596.
- Benedict, M., Lakshminarayan, V., Pino, J., & Chopra, I. (2016). Aerodynamics of a small-scale vertical-axis wind turbine with dynamic blade pitching. *AIAA Journal*, 54(3), 924–935, 00011452.

- Dunne, R., Schmid, P. J., & McKeon, B. J. (2016). Analysis of Flow Timescales on a Periodically Pitching/Surging Airfoil. *AIAA Journal*, *54*(11), 3421–3433, 0001-1452.
- Nguyen, L. & Metzger, M. (2017). Optimization of a vertical axis wind turbine for application in an urban/suburban area. *Journal of Renewable and Sustainable Energy*, *9*.
- Parker, C. M., Araya, D. B., & Leftwich, M. C. (2017). Effect of chord-to-diameter ratio on vertical-axis wind turbine wake development. *Experiments in Fluids*, *58*(12), 1–11, 07234864.
- Rezaeiha, A., Kalkman, I., & Blocken, B. (2017). Effect of pitch angle on power performance and aerodynamics of a vertical axis wind turbine. *Applied Energy*, *197*, 132–150, 03062619.
- Taira, K., Brunton, S. L., Dawson, S. T. M., Rowley, C. W., Colonius, T., McKeon, B. J., Schmidt, O. T., Gordeyev, S., Theofilis, V., & Ukeiley, L. S. (2017). Modal Analysis of Fluid Flows: An Overview. *55*(12), 4013–4041, 0001-1452.
- Buchner, A. J., Soria, J., Honnery, D., & Smits, A. J. (2018). Dynamic stall in vertical axis wind turbines: Scaling and topological considerations. *Journal of Fluid Mechanics*, *841*, 746–766, 14697645.
- Rezaeiha, A., Montazeri, H., & Blocken, B. (2018). Characterization of aerodynamic performance of vertical axis wind turbines: Impact of operational parameters. *Energy Conversion and Management*, *169*, 45–77, 0196-8904.
- Rolin, V. F. & Porté-Agel, F. (2018). Experimental investigation of vertical-axis wind-turbine wakes in boundary layer flow. *Renewable Energy*, *118*, 1–13, 18790682.
- Ayati, A. A., Steiros, K., Miller, A. M., Duvvuri, S., & Hultmark, M. (2019). A double-multiple streamtube model for vertical axis wind turbines of arbitrary rotor loading. *Wind Energy Science*, *4*(4), 653–662, 23667451.
- Coleman, D. G., Thomas, F. O., Gordeyev, S., & Corke, T. C. (2019). Parametric Modal Decomposition of Dynamic Stall. *AIAA Journal*, *57*(1), 176–190, 0001-1452.
- De Tavernier, D., Ferreira, C., & Van Bussel, G. (2019). Airfoil optimisation for vertical-axis wind turbines with variable pitch. *Wind Energy*, 10954244.
- Deparday, J. & Mulleners, K. (2019). Modeling the interplay between the shear layer and leading edge suction during dynamic stall. *Physics of Fluids*, *31*(10), 107104, 10897666.
- Ross, H. & Polagye, B. (2020). An experimental assessment of analytical blockage corrections for turbines. *Renewable Energy*, *152*, 1328–1341, 18790682.
- Dave, M. & Franck, J. A. (2021). Comparison of RANS and LES for a cross-flow turbine in confined and unconfined flow. *Journal of Renewable and Sustainable Energy*, *13*(6), 064503, 19417012.
- Dave, M., Strom, B., Snortland, A., Williams, O., Polagye, B., & Franck, J. A. (2021). Simulations of intracycle angular velocity control for a crossflow turbine. *AIAA Journal*, *59*(3), 812–824, 1533385X.
- Le Fouest, S., Deparday, J., & Mulleners, K. (2021). The dynamics and timescales of static stall. *Journal of Fluids and Structures*, *104*, 103304, 10958622.
- Menon, K. & Mittal, R. (2021). Significance of the strain-dominated region around a vortex on induced aerodynamic loads. *Journal of Fluid Mechanics*, *918*, R3, 0022-1120.
- Miller, M. A., Duvvuri, S., & Hultmark, M. (2021). Solidity effects on the performance of vertical-axis wind turbines. *Flow*, *1*, 1–9, 2633-4259.
- Wei, N. J., Brownstein, I. D., Cardona, J. L., Howland, M. F., & Dabiri, J. O. (2021). Near-wake structure of full-scale vertical-axis wind turbines. *Journal of Fluid Mechanics*, *914*, 17, 0022-1120.
- Ayancik, F. & Mulleners, K. (2022). All you need is time to generalise the Goman–Khrabrov dynamic stall model. *Journal of Fluid Mechanics*, *942*, R8, 0022-1120.
- Kiefer, J., Brunner, C. E., Hansen, M. O., & Hultmark, M. (2022). Dynamic stall at high Reynolds numbers induced by ramp-type pitching motions. *Journal of Fluid Mechanics*, *938*, A10, 0022-1120.
- Le Fouest, S. & Mulleners, K. (2022). The dynamic stall dilemma for vertical-axis wind turbines. *Renewable Energy*, *198*, 505–520, 0960-1481.
- Strom, B., Polagye, B., & Brunton, S. L. (2022). Near-wake dynamics of a vertical-axis turbine. *Journal of Fluid Mechanics*, *935*(6), 1–27, 0022-1120.
- Dave, M. & Franck, J. A. (2023). Analysis of dynamic stall development on a cross-flow turbine blade with modal decomposition. *arXiv*.

A. Appendix

A.1. Vertical-axis wind turbine model

A scaled-down model of a single-bladed H-type Darrieus wind turbine was mounted in the centre of the test section. The turbine has variable diameter D that was kept constant here at 30 cm. Up to three blades can be attached to the rotor arms through straight shafts that are held from the top. Here, we used the single-blade configuration to focus on the flow development around the blade in the absence of interference from the wakes of other blades. The turbine blade itself was 3D printed using a photosensitive polymer resin (Formlabs Form 2 stereolithography), sanded with very fine P180 grit paper and covered with black paint. The blade has a NACA0018 profile with a span of $s = 15$ cm and a chord of $c = 6$ cm, yielding a chord-to-diameter ratio of $c/D = 0.2$. The turbine blade is fully submersed and its top is located at $h_0 = 12$ cm below the water level. This yields a Froude number $Fr = \frac{U_\infty}{\sqrt{gh_0}} \in [0.26 - 0.65]$ for our tested range of tip-speed ratio $\lambda \in [1.2 - 3]$.

The turbine's compact geometry allowed for a blockage ratio of 12.5 %, based on the ratio of the turbine's swept area, given by the blade's span times the rotor diameter, and the water channel's cross-section. The blade is held by a cantilevered shaft such that there is no central strut interference with the flow. At low tip-speed ratios, the effective blockage is closer to 2.5 %, which is the blockage ratio calculated based on the ratio of the blade area, given by the blade's chord times its span, to the cross-sectional area. Additionally, a 2.5 chord length distance to the water channel's side walls is also respected at all times. Based on these observations, we consider the blockage and confinement effects small, and we did not apply any blockage correction to the force measurements (Parker et al., 2017; Ross & Polagye, 2020). This assumption is supported by a numerical simulation of a single-bladed wind turbine with a 32 % blockage ratio conducted by Simão Ferreira et al. (2008).

The turbine model is driven by a NEMA 34 stepper motor with a 0.05° resolution for the angular position. The rotational frequency was kept constant at 0.89 Hz to maintain a constant chord-based Reynolds number of $Re_c = (\rho\omega Rc)/\mu = 50\,000$, where ρ is the density and μ the dynamic viscosity of water. To investigate the role of the tip-speed ratio in the occurrence of dynamic stall, we systematically vary the water channel's incoming flow velocity from 0.14 m/s to 0.70 m/s to obtain tip-speed ratios ranging from 1.2 to 6.

A.2. Load measurements

The blade shaft was instrumented with twenty strain gauges forming five full Wheatstone bridge channels to record unsteady aerodynamic loads acting on the blade. The strain gauges are powered and their output signal is amplified using an instrumentation amplifier with precision voltage reference placed on a printed circuit board that is mounted directly on the rotor arm. The load cell was calibrated in situ using a fully orthogonal calibration rig and undergoing 1350 independent loading conditions. A calibration matrix was obtained by performing a linear regression on the calibration measurements. This matrix contained the 95 % confidence interval of the coefficients allowing an estimation of the uncertainty related to numerous factors, including response linearity, hysteresis, repeatability, and measurement error. The uncertainty was found to be below 5 % for the shear force and pitching moment components. A full description of the calibration procedure that includes the loading conditions, calibration matrix calculation, and error estimation can be found in the appendix of our previous work (Le Fouest & Mulleners, 2022).

For each experiment, the wind turbine model starts at rest with the blade facing the incoming flow. The turbine blade is then accelerated to its prescribed rotational speed. After reaching the target rotational speed, we wait for five full turbine rotations before starting the load recordings. Aerodynamic forces

acting on the turbine blade are recorded at 1000 Hz for 100 full turbine rotations, then the blade is brought to rest. The forces presented in this paper are the two shear forces applied at the blade's mid-span in the radial F_R and azimuthal F_θ direction, and the pitching moment about the blade's quarter-chord $M_{1/4}$. The total force applied to the blade is computed by combining the two shear forces: $F_{\text{tot}} = \sqrt{F_R^2 + F_\theta^2}$. All force coefficients are non-dimensionalised by the blade chord c , the blade span s , and the blade velocity $U_b = \omega R$ such that:

$$C_{\text{tot/R}/\theta} = \frac{F_{\text{tot/R}/\theta}}{0.5\rho U_b^2 s c} .$$

The subscripts tot, R, or θ refer to the total force, the radial, or the tangential force component. The centripetal force resulting from the turbine's rotation was experimentally measured by operating the wind turbine in air. The added drag from the two splitter plates was measured and offset for all investigated tip-speed ratios by operating the wind turbine without the blade, where the two splitter plates were held by a small cylinder. The influence of the centripetal force and the splitter plate are subtracted from the raw measurement data to isolate and compare the aerodynamic forces acting on the turbine blade. A more detailed description of the measurement and modelling of the non-aerodynamic forces is included in the appendix of our previous work (Le Fouest & Mulleners, 2022). The presented force data was filtered using a second-order low-pass filter with the cut-off frequency at 30 Hz. This frequency is multiple times larger than the pitching frequency and approximately 50 times larger than the expected post-stall vortex shedding frequency based on a chord-based Strouhal number of 0.2 (Roshko, 1961).

A.3. Particle image velocimetry

High-speed particle image velocimetry (PIV) was used to measure the flow field around the wind turbine blade. A dual oscillator diode-pumped ND:YLF laser ($\lambda = 527$ nm) with a maximum pulse energy of 30 mJ and a beam splitter were used to create two laser sheets from opposite sides of the channel. The light sheets were oriented horizontally at mid-span of the turbine blade. A high-speed camera with a sensor size of 1024 px \times 1024 px (Photron Fastcam SA-X2) and a spinning mirror apparatus were installed below the channel to capture the flow around the blade. The spinning mirror apparatus comprises two rotating and one stationary mirror, all oriented with a 45° angle with respect to the horizontal plane. The two moving mirrors rotate about the same axis of rotation and at the same frequency as the wind turbine. One of the mirrors is placed at the same radius as the model blade, such that it keeps the blade in the field of view of the camera at all times. The spinning mirror apparatus allows us to measure the velocity field around the blade with a higher spatial resolution and without scarifying the temporal resolution. The field of view is 2.5 $c \times$ 2.5 c centred around the blade. The acquisition frequency is 1000 Hz. The images were processed following standard procedures using a multi-grid algorithm (Raffel et al., 2007). The final window size was 48 px \times 48 px with an overlap of 75 %. This yields a grid spacing or physical resolution of 1.7 mm = 0.029 c . A window overlap above 50 % was selected to minimise spatial averaging of the velocity gradients by the interrogation window following Richard et al. (2006); Kindler et al. (2011). The out-of-plane vorticity component was calculated from the in-plane velocity components using a central difference scheme. Outliers were identified and removed based on a vorticity threshold and median filter. A missing-vector rate of 2 % was estimated across the different measurements series.

Due to the unsteady effective flow condition experienced by the blade throughout each rotation, the particle displacement between consecutive camera images varies greatly. To have sufficient particles displacement between correlated images and similar relative displacements errors at all azimuthal rotor positions, we have used a variable image skip. We have skipped a different number of particle images depending on the expected flow velocities at a given location and experimental conditions. The number of images skipped between the correlated images was determined based on the expected particle

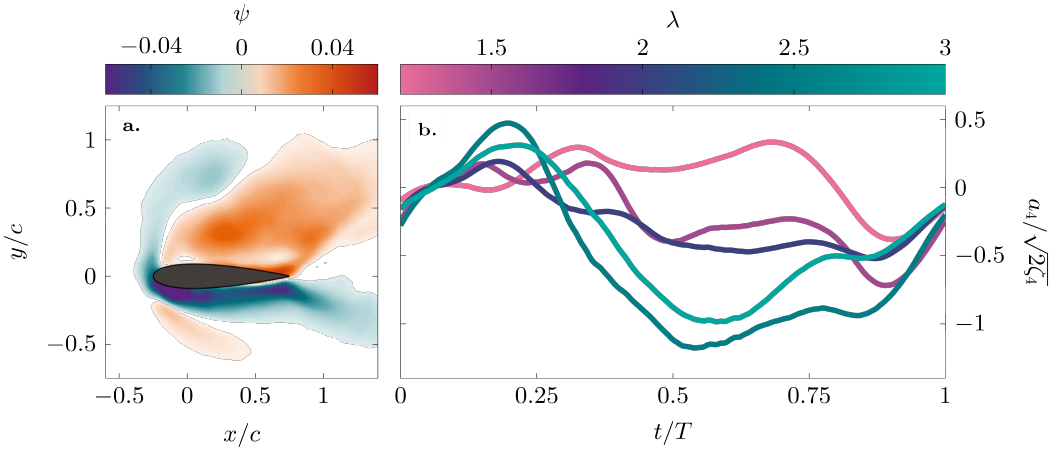


Figure 11. (a) Fourth spatial POD mode and (b) the evolution of the corresponding time coefficients for tip-speed ratios $\lambda = 1.2, 1.5, 2.0, 2.5$ and 3.0 .

displacement assuming that the flow velocity away from the blade matches the effective flow velocity. When the blade is at an azimuthal location where the expected effective velocity is low, more images are skipped and the time delay between the correlated images is increased. When the blade is at an azimuthal location where the expected effective velocity is high, no or fewer images are skipped and the time delay between the correlated images is decreased. At all positions, we aimed for a minimal partial displacement of 12 px when the flow moves with the nominal effective velocity.

A.4. Phase-averaging

Load measurements were obtained and phase-averaged over 100 wind turbine revolutions for all tip-speed ratio cases. Phase-averaging involves splitting the phase space into 540 bins that cover 0.67° without overlap. For each bin, we calculate the mean performance value and its standard deviation. This method allows us to visualise the mean performance of the turbine blade at 540 phase positions and the corresponding cycle-to-cycle variations of the performance. The number of bins was selected to be large enough such that sufficient data points lie in each bin and small enough to reduce the smoothening of the data. The acquired data and bin size yielded converged average and first-order statistical metrics of the unsteady aerodynamic loads experienced by the blade.

In addition to the load measurements, we conducted time-resolved velocity field measurements using PIV for the tip-speed ratios $\lambda \in \{1.2, 1.5, 2, 2.5, 3\}$. For every tip-speed-ratio, we collected a total of 21 838 instantaneous particle images at an acquisition rate of 1000 Hz. The images have been pairwise correlated using variable image gaps to obtain instantaneous velocity fields. These instantaneous velocity fields were then divided into 200 bins that each cover 1.8° without overlap. The same azimuthal resolution is used for all tip-speed-ratios. The azimuthal resolution for the velocity field phase-averaging is smaller than for the load phase-averaging. The velocity fields were recorded for 21 turbine rotations. The load data was recorded for 100 rotations. The rotational velocity of the turbine was 0.89 Hz for all tip-speed-ratios as the tip-speed-ratio was altered by changing the incoming flow velocity.

Proper orthogonal decomposition is applied on the resulting phase-averaged flow fields. This operation drastically decreases the computational cost, which scales with the number of snapshots squared.

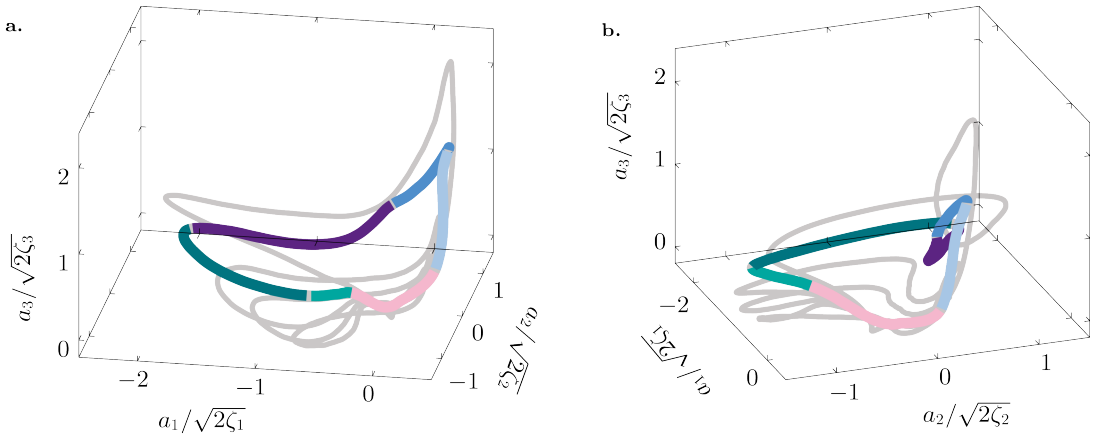


Figure 12. Time coefficient parametric curve obtained from the stacked vorticity field POD, similar to figure 6a in the manuscript, but under two different orientations. The curve corresponding to tip-speed ratio $\lambda = 1.5$ is highlighted.

A.5. Fourth POD mode

The first three spatial POD modes and the corresponding time coefficients for tip-speed ratios $\lambda = 1.2, 1.5, 2.0, 2.5$ and 3.0 are included in the main manuscript. They have been used to identify the dynamic stall development stages.

The fourth POD mode, which plays a more prominent role than the third mode for higher tip-speed ratios where stall is less prominent, did not provide additional information for the identification of the stall stages. It is shown in figure 11 for reference.

The fourth spatial mode represents the second leading-edge vortex that forms in the downwind half. The time coefficients indicating the contribution of the fourth POD mode reach higher values for the higher tip-speed ratios ($\lambda = 2, 2.5,$ and 3) than for the low tip-speed ratio ($\lambda = 1.2$ and 1.5). For low tip-speed ratios, the downwind half is mostly dominated by deep post-stall conditions and fully separated flow, whereas the higher tip-speed ratio cases are generally able to recover and form a second coherent leading-edge vortex, yielding an improved efficiency.

A.6. Alternative viewing angles of the time coefficient parametric curves

The stage detection is based on inflection points in the three-dimensional parametric curves. Depending on the orientation of the plot, not all inflection points are clearly visible. Additional views are presented in figure 12.